

See discussions, stats, and author profiles for this publication at: <https://www.researchgate.net/publication/262860630>

High Temperature Crystallization of Free-Standing Anatase TiO₂ Nanotube Membranes for High Efficiency Dye-Sensitized Solar Cells

ARTICLE in ADVANCED FUNCTIONAL MATERIALS · DECEMBER 2013

Impact Factor: 11.81 · DOI: 10.1002/adfm.201301066

CITATIONS

22

READS

32

9 AUTHORS, INCLUDING:



Min Guo

National Huaqiao University

16 PUBLICATIONS 149 CITATIONS

[SEE PROFILE](#)



Wei Lu

The Hong Kong Polytechnic University

85 PUBLICATIONS 766 CITATIONS

[SEE PROFILE](#)



Guoge Zhang

14 PUBLICATIONS 309 CITATIONS

[SEE PROFILE](#)



Haitao Huang

The Hong Kong Polytechnic University

176 PUBLICATIONS 2,778 CITATIONS

[SEE PROFILE](#)

High Temperature Crystallization of Free-Standing Anatase TiO_2 Nanotube Membranes for High Efficiency Dye-Sensitized Solar Cells

Jia Lin, Min Guo, Cho Tung Yip, Wei Lu, Guoge Zhang, Xiaolin Liu, Limin Zhou, Xianfeng Chen,* and Haitao Huang*

Despite the one-dimensional ordering of anodic TiO_2 nanotube arrays (TNAs), the electron diffusion towards the substrate in TNA-based dye-sensitized solar cells (DSSCs) is comparably slow. The improvement of electron mobility by enhancing TNA crystallinity under high-temperature annealing, however, is infeasible with the existence of Ti metal substrate. Herein, it is shown that, by high temperature (up to 700 °C) crystallization of high-quality free-standing TNA membranes, the TNAs can maintain their structure integrity and phase (anatase) stability as a result of the absence of the nucleation sites and the high quality of the membrane obtained by a self-detachment method. The electron transport is much faster (~4 times) in the 700 °C-annealed TNA membranes than that in the 400 °C-treated ones for 20 μm-length nanotubes, which is mainly attributed to the improved crystallinity and reduced electron trap states. In spite of slightly reduced dye loading capacity (decreased by ~30%) in the 700 °C-annealed membranes, the superior electron transport leads to a significantly improved efficiency of 7.81% (enhanced by ~50%). The strategy of manipulating the electron transport dynamics by high temperature treatment on high-quality TNA membranes may open new route for further improvement in the performances of TNA-based DSSCs.

1. Introduction

One-dimensional TiO_2 nanotube arrays (TNAs) prepared via electrochemical anodization have attracted much attention for use as the photoanodes of dye-sensitized solar cells (DSSCs).^[1–5] As compared with the randomly packed and disordered TiO_2 nanoparticle (TNP) networks with numerous particle–particle interfaces, the “vectorial transport” of photogenerated electrons along the TNA tube walls was thought to lead to higher charge mobility, which is crucial for the improvement of DSSC performances.^[6–10] Recent studies have, in fact, demonstrated that the electron transport in typical TNAs is as slow as that in TNP films, although the underlying mechanisms are quite different (exciton-like trap states in TNA films and structural disorder in TNP films).^[11–13] As a result of the existence of these states, which suppresses the electron mobility, the improvement of TNA-based DSSCs is limited and the highest efficiency of DSSCs consisting of the

pure TNAs (without further surface treatment) is only about 5% (around 7–9% for mixed systems), which is still lower than that achieved with the TNPs.^[1,14]

Crystallization by thermal annealing at high temperature in oxidative atmosphere is an effective way to enhance the electron mobility in TNAs, since the annealing leads to lowered density of both bulk and surface trap states by reducing the number of defects and oxygen vacancies/ Ti^{3+} existing in the band gap induced by amorphous domains, grain boundaries, and impurities embedded during anodization.^[12,15] However, investigations show that the photoanodes consisted of TNAs attached to Ti substrate (TNAs-Ti) exhibit the highest efficiency at relatively low annealing temperatures ranging from 400 to 500 °C (with the pure anatase crystal phase).^[16,17] The efficiency decreased markedly with further increase in the annealing temperature due to the “substrate effect”—the Ti substrate which supports TNA overlayer greatly influences the crystallization process. As the metallic Ti substrate is directly oxidized to rutile, a thin compact (rutile) layer at the interface region forms, and gradually becomes thicker.^[17–19] This initiates the geometry change and phase transformation of the

Dr. J. Lin, X. L. Liu, Prof. X. F. Chen
Department of Physics

State Key Laboratory of Advanced Optical Communication Systems and Networks

Shanghai Jiao Tong University
Shanghai 200240, China
E-mail: xfchen@sjtu.edu.cn

Dr. J. Lin, M. Guo, C. T. Yip, W. Lu, Dr. G. Zhang, Prof. H. Huang
Department of Applied Physics and Materials Research Center

The Hong Kong Polytechnic University
Hung Hom, Kowloon, Hong Kong
E-mail: aphuang@polyu.edu.hk

Dr. G. Zhang
School of Materials Science and Engineering
South China University of Technology
Guangzhou, China

Prof. L. Zhou
Department of Mechanical Engineering
The Hong Kong Polytechnic University
Hung Hom, Kowloon, Hong Kong

DOI: 10.1002/adfm.201301066



TNAs, from the substrate to the top side. This substrate effect of TNA-Ti samples is severe and occurs at various annealing conditions.^[20–22] In fact, in literature reports, the temperature at which rutile can be detected, and also the fraction of rutile, vary greatly due to the difference in the nanotube layer thickness. As rutile is thermally grown from the underlying substrate, the detection becomes increasingly difficult for longer tubes (at 500–550 °C for thick TNA layers^[16,17,21] and 400–450 °C for thin TNA layers^[23]). Furthermore, the TNA layer is gradually densified from the interface, accompanied by dramatically lowered surface area, and gradually disappearing tube structure. The complete compactization occurs at 700 °C for short tubes^[20] and 750–800 °C for micrometer-long tubes^[24,25] with annealing duration of 1–2 h. The substrate effect, connected with the compact rutile layer at the interface between TNAs and Ti substrate, introduces a strong increase of the resistance and structural destruction under high annealing temperatures, which hinders the electron transport to the external circuit and reduces the available internal surface areas, respectively, both detrimental to DSSCs. Thus, eliminating the influence of the underlying rutile layer is essential for DSSC applications using TNA photoanodes.

In order to eliminate the substrate effect at high temperatures, thus enhancing the DSSC performance, several attempts have been tried to detach the TNAs from the Ti substrate and anneal them at high temperatures^[26–28] before being transferred to a fluorine doped tin oxide (FTO) glass substrate to form the photoanode. However, those free-standing TNA membranes were easily broken and no intact membranes were obtained. To obtain high-quality TNA membranes without any crack, a self-detaching method^[29] was developed, avoiding additional ultrasonication or acid treatment steps to peel off the TNA membranes from the Ti metal substrate. Based on the high quality and flexible manipulation of the self-detached TNA membranes, we have already created the periodically structured TNA films, and coupled these membranes to DSSCs.^[30–32] Here, we find that these high-quality TNA membranes can maintain phase stability (anatase) and structural integrity under high temperature crystallization (up to 700 °C, much higher than the commonly used crystallization temperatures). The crystallized TNA membranes were used as photoanodes of DSSCs and, as benefited from the substantial improvement in the efficiency of electron transport after the elevated temperature crystallization, the photovoltaic conversion efficiency (PCE) of DSSC was improved significantly ($\approx 50\%$), reaching a value as high as 7.81% (with the best efficiency over 8%).

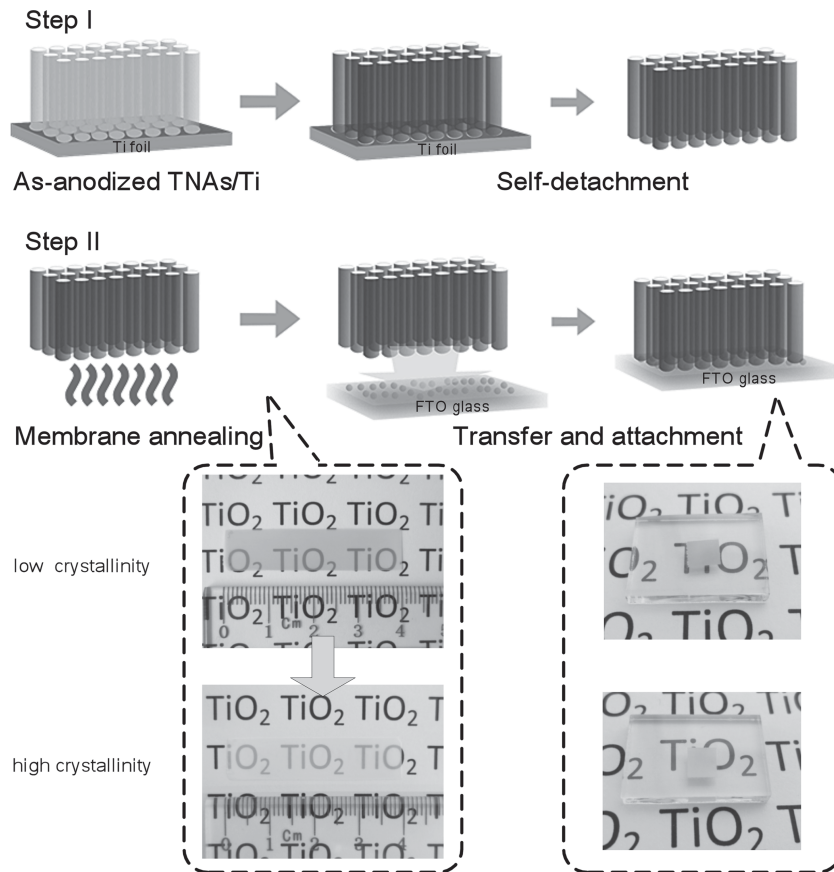


Figure 1. Schematic diagram of the detaching and transfer process of the TNA membrane and photographs of the large-area as-detached membrane (400 °C annealed) and high temperature crystallized (700 °C annealed) membrane, showing the slight color change of the TNA membranes. The right column shows the integrated photoanode with membranes attached to the FTO substrate.

2. Results and Discussion

The fabrication sequence of the self-detached TNA membrane photoanode for DSSCs is shown in Figure 1. This process mainly includes two steps: I) high-quality TNA membranes were obtained by self-detachment (see the Experimental Section) during the fabrication of anodic TNAs with different thicknesses, and II) the free-standing TNA membranes were annealed at different temperatures and then reliably attached onto FTO glass substrates by thin layers of TNPs, forming the photoanodes for front-side illuminated DSSCs. It is noteworthy that during the high temperature crystallization process, the large-area free-standing TNA membrane maintained the high quality with no cracks (Figure 1, bottom). The photograph of the integrated photoanodes is also shown.

The grains at the tube sidewalls of the TNAs were found to be gradually coarsened with increased temperatures, showing microcracks at the grain boundaries (Figure 2a–d). This variation of wall morphology has been observed to appear at a temperature as low as 450 °C.^[23] However, as the further grain growth was constrained by the tube borders, the aligned tube structure and the overall regular morphology of TNAs were retained during annealing process at a higher temperature.

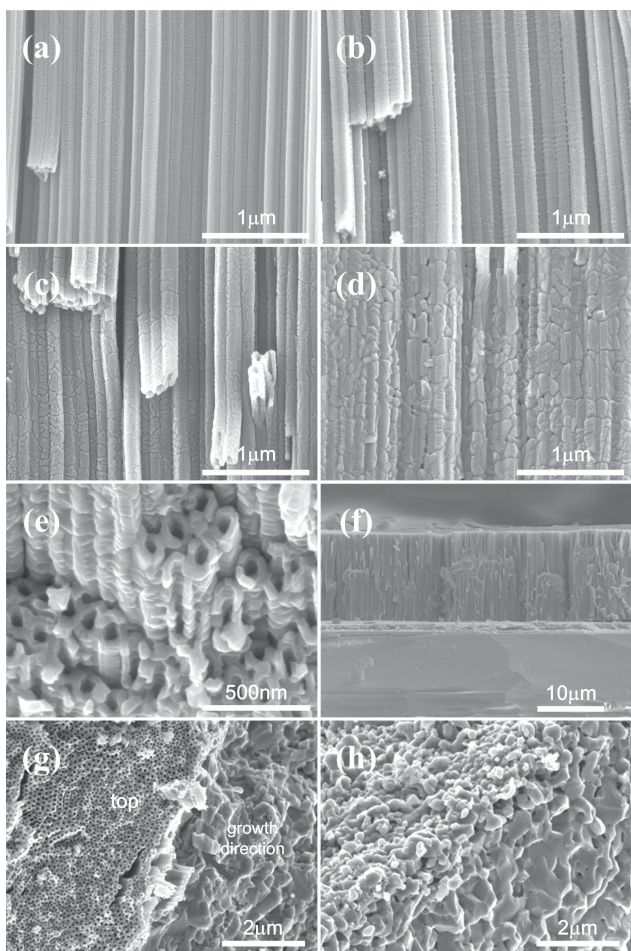


Figure 2. Field-emission scanning electron microscopy (FESEM) images of a) 500, b) 600, c) 700, and d) 800 °C-annealed samples showing the morphological evolution. e) The enlarged view of the TNA structure annealed at 800 °C. f) The sideview of the photoanode consisted of the 700 °C-annealed TNA membrane. The densification of the tubes from the bottom to the top side: g) partial densification and h) full densification.

Figure 2e shows the close-up image of the inner part of TNAs. After annealing at 800 °C, the outside tube wall appeared to be layered and corrugated, and started to coalesce together, while the inner channels remained open, with the ordered pore morphology. The transmission electron microscopy (TEM) images in Figure 3 show that during the crystal growth, TNAs kept the tube morphology in the entire temperature region and the tube wall became thicker (from ≈ 10 to 20 nm), leading to a reduction of the inner surface area to a certain extent. The annealed TNA membranes with excellent quality were successfully integrated to FTO substrate for DSSCs. The cross-sectional view of the photoanode consisted of 700 °C-annealed, 13 μm -thick TNAs and a thin TNP adhesion layer of $\approx 1 \mu\text{m}$ is shown in Figure 2f, revealing tight attachment of TNAs to the FTO glass. Compared with the TNA-Ti samples with severe densification of tubes from the bottom to the top, and eventually disappeared tube geometry by transforming into a compact layer (Figure 2g,h), the destruction of the nanotubes under high temperature annealing was prevented by eliminating the

substrate effect. By using this configuration, the highly crystallized TNA membrane-based photoanode can be synthesized by the high temperature annealing process.

The TNA membranes maintained in anatase phase when annealed at 400–700 °C, and rutile started to emerge in the 800 °C-annealed membranes (Figure 4a). For the membrane annealed at 800 °C, 2.7% rutile was estimated from X-ray diffraction (XRD) on the top side, while the rutile peak was more evident at the bottom (rutile fraction 16.7%, Figure 4a inset). This indicates that in the absence of the Ti substrate, rutile also started to form from the bottom side of TNAs, where more densely packed tubes and thicker tube walls were found. For 700 °C-annealed membranes, no rutile peak was found on both sides of the membrane, indicating the tubes in pure anatase phase. The phase transition temperature of free-standing TNAs was also demonstrated to be >600 °C in their powder form.^[17] For comparison, the phase stability of TNPs (≈ 20 nm size, coated on quartz glass) and TNAs-Ti was investigated under the same condition. Both anatase and rutile phases were found in 600 °C-annealed TNP and TNA-Ti samples (Figure S1 and Table S1, Supporting Information). When annealed at 800 °C, the TNPs completely transformed from anatase to rutile, and the fraction of rutile in TNAs-Ti was as high as 38.6%. The gradual narrowing of the prominent anatase (101) diffraction peaks and the increasing of peak intensity of TNA membranes with increasing annealing temperatures mean larger crystalline sizes and better crystallinity (Figure S2, Supporting Information). The crystalline sizes of TNA membranes, TNPs and TNAs-Ti are summarized in Table S1, Supporting Information. For TNA membranes, the average grain size slowly increased from 27.5 to 34.2 nm (increased by 24%) at 400–800 °C. Actually, the sidewall is consisted of elongated grains aligned along the tube axis with lengths >100 nm (TEM image in Figure 3f). In the case of TNPs, significant enlargement of the crystalline size was observed (13.7–22.6 nm at 400–700 °C, increased by 65%).

Figure 4b is the high-resolution Raman spectra in the range of 100–180 cm^{-1} , showing the lowest-frequency E_g mode of anatase arising from the external vibration. It is apparent that with increasing annealing temperatures from 400 to 800 °C, the Raman spectra narrowed significantly and corresponding peak intensities increased. This implies that the crystallinity was greatly enhanced by raising the annealing temperatures and the number of oxygen vacancies in the TNA films was greatly decreased.^[33,34] The variation of the oxygen vacancy number was further demonstrated by XPS measurement (Figure S3, Supporting Information). The main peak of O1s core level spectra, which was located at 529.7–529.8 eV, is similar for both annealing temperatures. A decrease of the intensity at 531.5 eV, after annealing at 800 °C, could be attributed to the decreased number of oxygen vacancies/Ti³⁺ states in the surface regions.^[15]

The photocurrent density-voltage ($J-V$) characteristics of DSSCs based on TNA membranes annealed at 400–800 °C are shown in Figure 5 and Table 1. With the retarded phase transformation in TNA membranes, the short-circuit current density (J_{sc}) increased with increasing annealing temperatures from 400 to 700 °C and then decreased at 800 °C for 20 μm TNAs (Figure 5b). The open-circuit voltage (V_{oc}) increased in

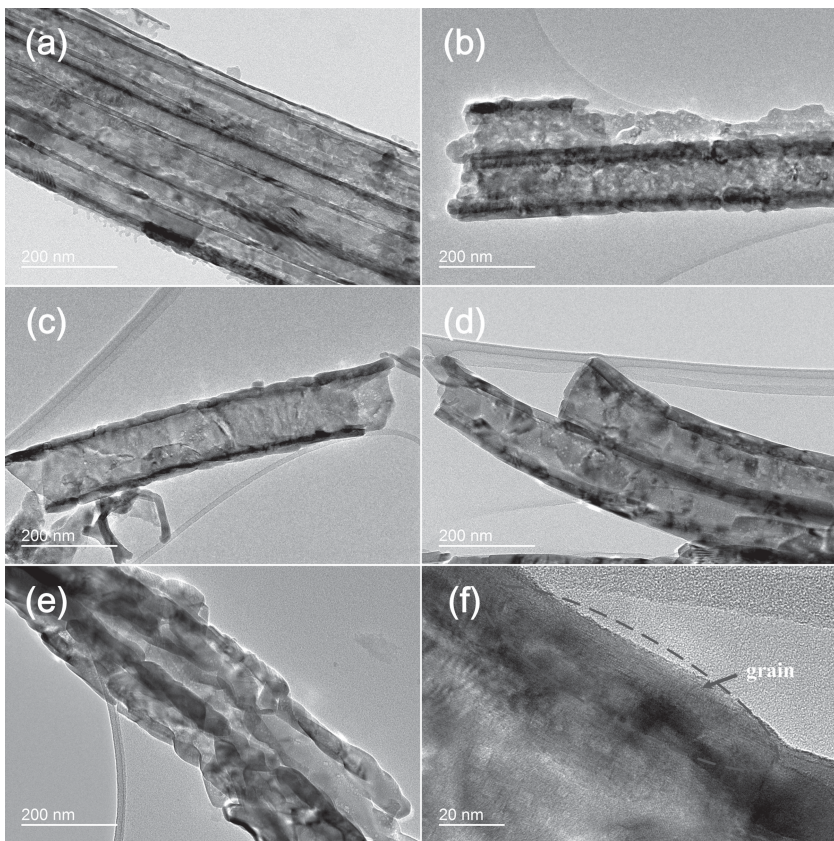


Figure 3. TEM images of a–e) TNAs annealed at 400–800 °C and f) high-resolution view of the grain in the tube wall at 700 °C.

the whole temperature range, from 0.71 V at 400 °C to 0.76 V at 800 °C, with a 50 mV increment. As annealing itself has negligible effect on the intrinsic energy band structure of anatase TiO_2 , the enhancement could be ascribed to the decreased trap densities. In the entire range the fill factor (FF) changed slightly, due to the comparable overall series resistances. The incident photon to current conversion efficiency (IPCE) spectra are also shown and provide further evidence to the photocurrent enhancement (Figure S5, Supporting Information). It can be found that the high temperature crystallization significantly increases the IPCE over the entire visible wavelength range. As a result of the enhancement in both J_{sc} and V_{oc} , the overall PCE at 700 °C reached the maximum value of 7.81% for 20 μm TNAs (Figure 5c, a high value for TNA-based DSSCs without TiCl_4 treatment). Compared with 400 °C-annealed samples, the values of PCE increased by $\approx 50\%$. The better performance should directly result from the higher crystallinity of the nanotubes sintered at a higher temperature. At the highest annealing temperature of 800 °C, the PCE started to decrease. However, the value was still relatively high (PCE = 6.16%). As mentioned above, at 800 °C, the tube structure started to collapse and the rutile phase emerged, resulting in smaller surface area and lower electron conductivity. Moreover, we also fabricated TNA-based DSSCs with different lengths annealed at the temperature of 700 °C. By further increasing the thickness of the TNA layer (up to $\approx 50 \mu\text{m}$ with intact top surface),^[35] a

maximum efficiency of 8.00% was obtained at a tube length of $\approx 30 \mu\text{m}$ (Figure S6,S7 and Table S2, Supporting Information), which is thicker than conventional low-crystallinity tube layers suitable for DSSCs (≈ 15 – $20 \mu\text{m}$). The J_{sc} first increased with longer tubes and then slowly decreased, and V_{oc} continuously decreased, as a result of the competition between enhanced light harvesting and recombination.

As discussed above, direct annealing of TNAs-Ti samples leads to the densification of upper TNA layer and significantly lowered surface areas (close to 100% at high temperatures, Figure 2h). In contrast, as the TNA membranes maintain the regular morphology of aligned tubes and porous structures, the variation of the surface area is much smaller. **Figure 6a** compares the adsorption–desorption isotherms and corresponding pore size distribution of the TNA membranes annealed at low and high temperatures (400 and 800 °C). By increasing the annealing temperature, the loops shift to the higher relative pressure (P/P_0) region while the loop position gradually decreases, indicating the decreased surface areas of the TNA films. The Brunauer–Emmett–Teller (BET) specific surface area slowly decreased from 20.09 $\text{m}^2 \text{ g}^{-1}$ at 400 °C to 13.60 $\text{m}^2 \text{ g}^{-1}$ at 800 °C, a reduction by a factor of 32%. The pore sizes show similar wide distributions over the range of 10–100 nm, indicating that

no severe aggregation and collapse of tubes occurs during the high temperature crystallization. This is consistent with the dye loading measurement, which shows that the adsorbed amounts of dye molecules decreased by 30% for 20 μm TNAs (Figure 6b and Table 1). Considering the lower dye loading values and hence decreased light harvesting, a smaller J_{sc} would be expected. However, the J_{sc} values increased gradually with elevated temperature, indicating the presence of other dominant factors for higher J_{sc} values.

To better understand the underlying mechanisms, the electrochemical properties of the photoanodes with TNA membranes annealed at various temperatures were demonstrated by electrochemical impedance spectroscopy (EIS) measurement in the dark at different applied bias voltages. The impedance spectra were fitted by a transmission line model^[36] to determine the kinetics parameters describing the electron transfer and transport inside the DSSCs. The variation of the density of sub-bandgap traps was further confirmed by the chemical capacitance (C_μ) of the TNA films.^[37,38] **Figure 7a** shows C_μ as a function of applied bias voltage, which increases exponentially with increasing voltage. This is in accordance with the trap-limited transport model, since the density of traps is higher at the band edge and decreases exponentially towards the band gap. The curves for samples annealed at different temperatures show similar slopes over the bias range. The substantial decrease in the number of oxygen vacancies/ Ti^{3+} states,

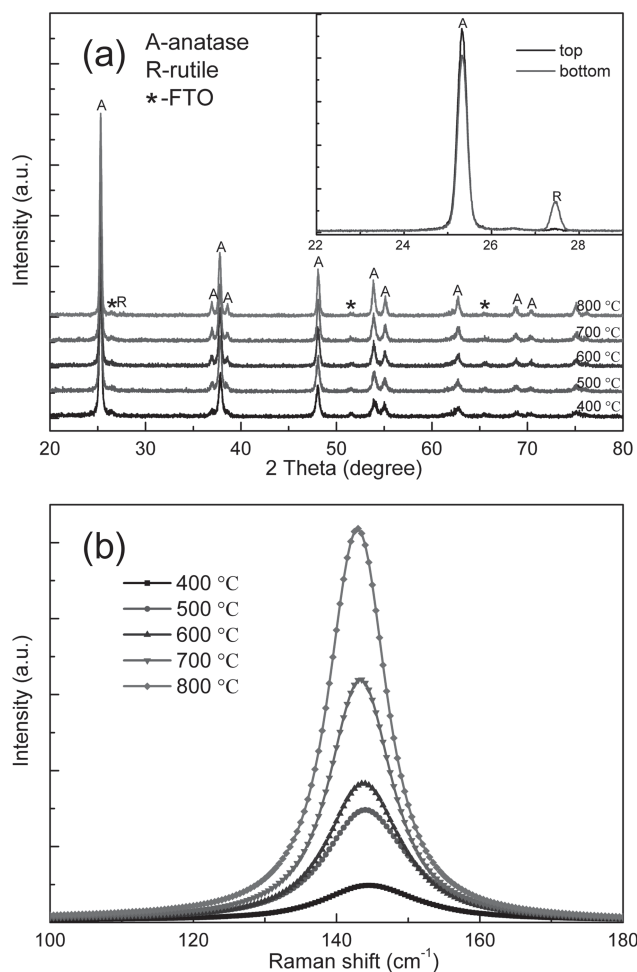


Figure 4. a) The XRD patterns of TNA membranes attached onto FTO. The inset compares the detailed XRD patterns at the top and bottom sides of the 800 °C-annealed free-standing membrane. b) Raman spectra of the lowest-frequency E_g mode in the TNA membranes.

as mentioned above, leads to enormously decreased C_μ values by $\approx 1/6$ (from 16.5 to 2.8 mF cm $^{-2}$ at 0.72 V) after the high temperature annealing of the TNA films. The slight increase of the crystalline size and decrease of surface area at elevated temperature may also contribute a small part to decreased trap sites. The improved crystallinity leads to a lower chance of electron recombination through surface trap sites, and consequently higher V_{oc} values. This is also obvious from the variation of the recombination resistance (R_{ct}), which is associated with the charge transfer process across the interface. The high temperature crystallized TNAs own larger R_{ct} (Figure 7b), and thus denotes slower recombination rate of the interfacial process. The transport resistance (R_t) of electron is comparable in all types of photoanodes (Figure 7c). The resistances of R_{ct} and R_t also show an exponential dependence on the bias voltage (inversely proportional to the electron concentration).

The electron properties were analyzed in terms of effective diffusion coefficient (D_n), recombination time (τ_n), and diffusion length (L_n), which are critical for the evaluation of the

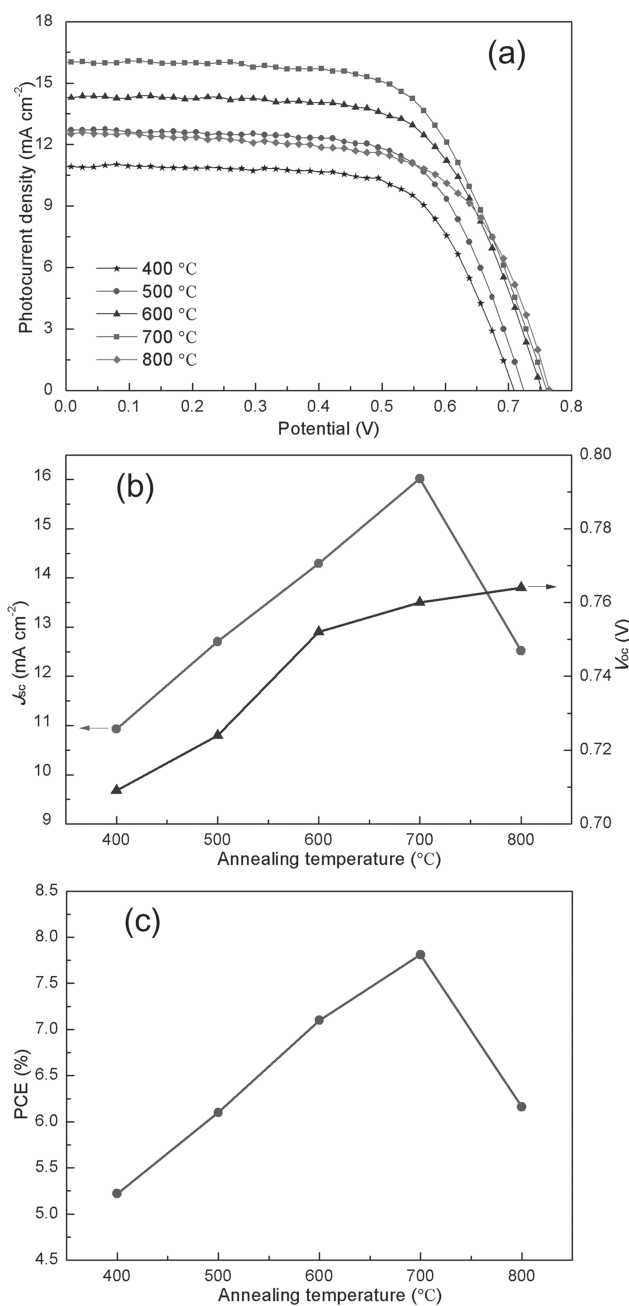


Figure 5. a) The J - V characteristics of DSSCs based on 20 μm -thick TNA membranes annealed at different temperatures. b,c) Photovoltaic parameters, including J_{sc} , V_{oc} , and PCE of DSSCs.

photovoltaic performance and can be calculated from the measured C_m , R_{ct} , and R_t as follows:^[36]

$$D_n = d^2 / (R_t C_\mu), \quad \tau_n = R_{ct} C_\mu, \quad L_n = (D_n \tau_n)^{1/2} \quad (1)$$

where d is the thickness of the film. For the same applied bias, the electron diffusion rate in the TNA membranes is greatly enhanced with increased crystallinity. The D_n increased from 1.4 to 6.1×10^{-4} cm 2 s $^{-1}$ at 0.72 V by increasing the annealing

Table 1. The photovoltaic parameters of DSSCs based on TNA membranes annealed at different temperatures and the dye amounts adsorbed by the photoanodes.

Temperature [°C]	J_{sc} [mA cm ⁻²]	V_{oc} [V]	FF	PCE [%]	Dye amount [10 ⁻⁷ mol cm ⁻²]
400	10.93	0.71	0.67	5.22	1.36
500	12.71	0.72	0.66	6.10	1.19
600	14.29	0.75	0.66	7.10	1.00
700	16.02	0.76	0.64	7.81	0.97
800	12.52	0.76	0.64	6.16	0.93

temperature from 400 to 700 °C (Figure 8b), which is a significant improvement (≈ 4 times). It is well-known that the photo-injected electrons in the conduction band normally undergo trap-mediated diffusion before reaching the collecting electrode.^[39,40] As a large number of electron traps exist in conventional low crystallinity TNAs, these states strongly influence the transport and recombination kinetics of the photoinjected electrons. The fewer traps throughout the electron pathways facilitate the electron movement in the conduction band with a

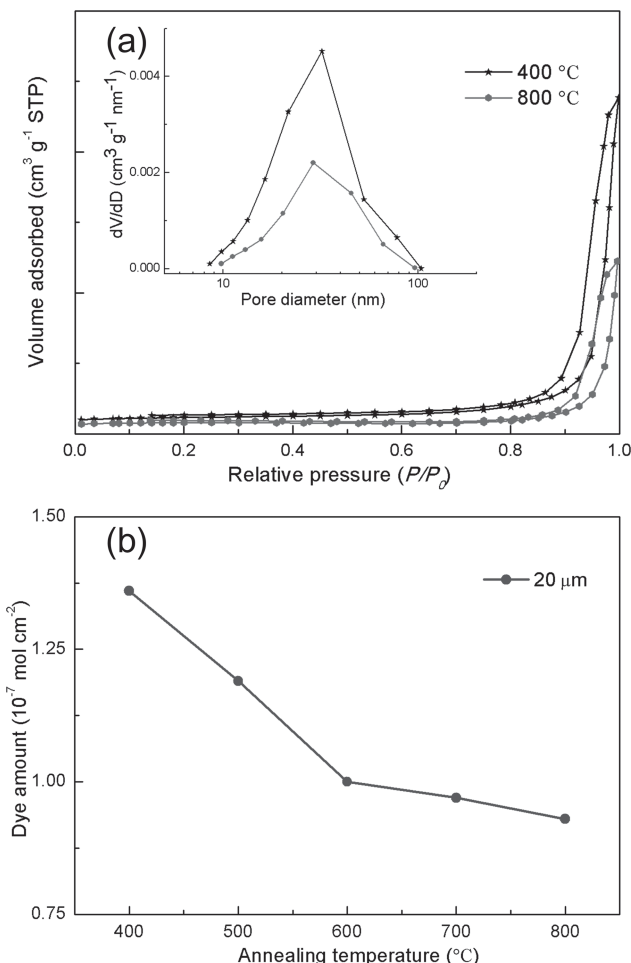


Figure 6. a) BET surface areas and pore size distribution. b) The variation of dye amounts adsorbed by the photoanodes.

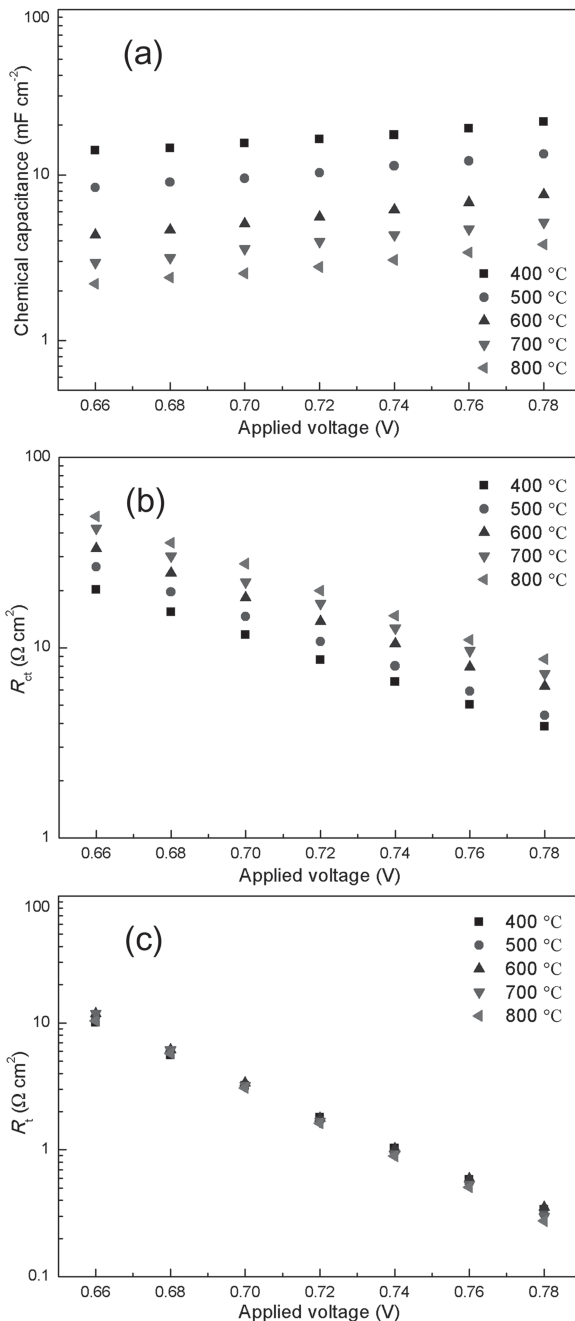


Figure 7. The kinetics parameters measured at different applied bias voltages: a) chemical capacitance, b) recombination resistance, and c) transport resistance. The data is obtained by fitting the EIS.

smaller number of trapping/detrapping events. This results in faster electron diffusion towards the substrate and thus higher J_{sc} in TNAs annealed at higher temperatures, as depicted in Figure 8a. The promoted electron diffusion in DSSCs, based on high temperature crystallized TNAs, was confirmed by the stepped light-induced transient photocurrent investigation (Figure S8, Supporting Information). It is noteworthy that the opposite trend of diffusion coefficient D_n under any photon

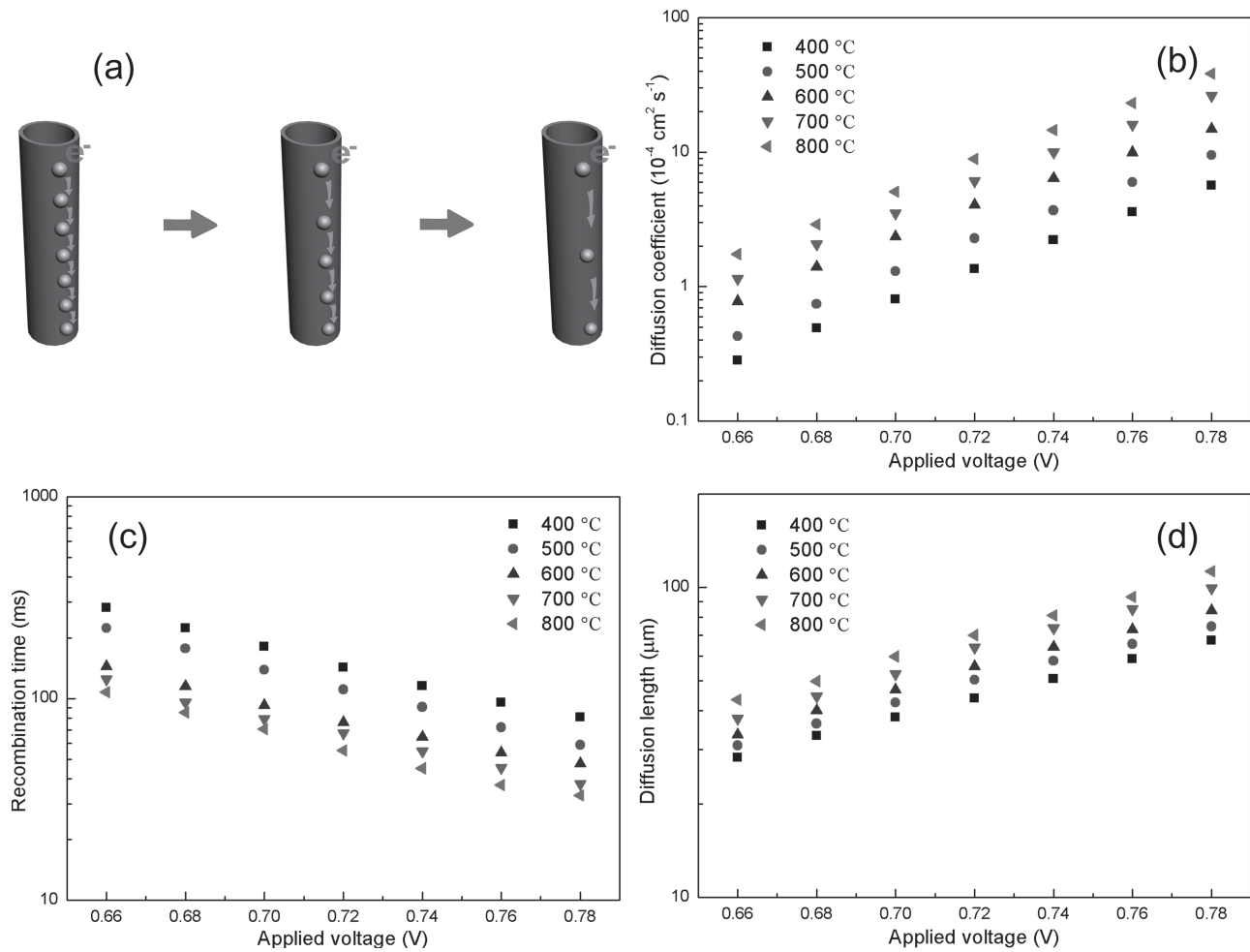


Figure 8. a) Schematic representation of the reduced traps for the faster electron diffusion. Comparison of b) diffusion coefficient, c) electron recombination time, and d) diffusion length of DSSCs as a function of the annealing temperature.

flux has been reported in the TNA–Ti systems,^[16,17] which may originate from the significantly slower electron transport through the rutile interface layer annealed at higher temperatures. As shown in Figure 8c, the apparent recombination time of the electrons (τ_n) with the tri-iodide ion at TiO_2 /electrolyte interfaces is shortened with the enhanced crystallinity, which is mainly due to the variation of trap densities. The decreased average response time of both trapped and untrapped electrons as measured, however, does not imply an enhancement in recombination flux. In fact, lower dark current was observed for TNAs crystallized at higher temperatures (Figure S9, Supporting Information). This is consistent with the above discussion that the probability of electron back transfer at the interface is lowered by reduced surface traps. Overall, by increasing the annealing temperature, the greatly decreased number of traps in the films leads to longer effective diffusion length of electrons as compared with low crystallinity TNAs (Figure 8d). The improved diffusion length is consistent with the above results that the effective tube layer becomes thicker under high temperature crystallization. For crystallization temperature up to 700 °C, the reduced trap density in the TNA film is the dominant factor (over the amount of dye-loading in this

case) influencing the performance of the DSSCs, while above that temperature, collapse of tube layers and lowering of surface area become more severe.

3. Conclusions

The structures, anatase to rutile phase transformation, photovoltaic performance, and electron transport and recombination dynamics of the front-side illuminated DSSCs were studied based on the high-quality self-detached TNA membranes. In comparison to TNAs–Ti, the self-detached TNA membranes demonstrated a much better thermal stability with the retention of tube geometry in the annealing temperature range of 400–800 °C, and only minor rutile phase appeared at 800 °C due to the removal of the “substrate effect”. The electron transport was much faster in the 700 °C-annealed TNA membranes than the 400 °C-treated ones (≈ 4 times), which was mainly attributed to the enhanced crystallinity and reduced number of electron trap states within the photoanodes under elevated annealing temperatures. As a result of the superior electron transport properties, the performance of TNA-based DSSCs was significantly

improved, and the 20 μm TNAs annealed at 700 °C showed the improved solar energy conversion efficiency of 7.81% (enhanced by \approx 50%, as compared with the one annealed at 400 °C). The excellent electron transport properties of the TNA membranes with high temperature annealing can be of great importance to the further improvement of the performance of TNA-based DSSCs and devices for other applications.

4. Experimental Section

Preparation of TNA Membranes: Self-detached free-standing TNA membranes (bottom closed) were synthesized as reported previously.^[29] Briefly, regular TNAs were synthesized by a two-step anodization of Ti foil (0.125 mm thickness, 99.7% purity, Strem Chemicals) at room temperature (\approx 20 °C) in an ethylene glycol electrolyte (containing 0.5 wt% NH₄F and 3 vol% water) at an applied potential of 60 V using a computer controlled sourcemeter (Model 2400, Keithley, USA). TNAs with different tube lengths were obtained by prolonged anodization. The as-anodized samples were annealed at 400 °C and then anodized again at 60 V and 35 °C for \approx 1–2 h (dependent on tube layer thickness) to detach the TNA membranes. The membranes were cleaned in ethanol repeatedly and then dried in air. After that, the crack-free membranes were annealed in the temperature range of 400–800 °C for 2 h in air with a heating and cooling rate of 3 °C min⁻¹. During the thermal treatment, upward curvaturating of the thin TNA membranes sometimes may occur and can be avoided by covering with quartz glasses.

Fabrication of DSSCs: The TNA membranes were attached to FTO glasses (15 Ω per square) coated with hydrothermally prepared anatase TNPs (average size 20 nm and thickness \approx 1 μm , as received from Wuhan Geao Instruments Science and Technology Co. Ltd., China) using a doctor-blade technique. The active area of the solar cells was 0.16 cm² (defined by a template) with the actual area of each cell measured separately and used for the calculation of short-circuit current. After dried under ambient conditions, they were annealed again at 400 °C for 2 h to ensure good electrical connectivity between TNA membranes and FTO substrate. Then the photoanodes were immersed in dye solution (N719, 0.3 mm in ethanol, Solaronix) at room temperature for 24 h. A sandwich-type configuration was employed with a hot-melt spacer (SX1170, 25/60 μm thickness, Solaronix) and Pt coated FTO glass (by thermal decomposition of H₂PtCl₆/isopropanol solution at 380 °C for 30 min) as the counter electrode. The interspace of the DSSCs was filled with a liquid electrolyte (1.0 M 1,2-dimethyl-3-propyl imidazolium iodide (DMPII), 0.12 M diiodine (I₂), 0.1 M lithium iodide (LiI), and 0.5 M 4-tert-butylpyridine (TBP) in 3-methoxypropionitrile (MPN)).

Characterizations: The surface area was characterized by BET analysis via N₂ adsorption-desorption isotherm (ASAP 2020, Micromeritics Instruments, USA). The dye amount was measured by desorbing the anchored dye in 0.1 M NaOH aqueous solution, and the absorbance was measured by UV-vis spectrophotometer (Model UV-2550, Shimadzu, Japan). X-ray diffraction analysis (XRD, Rigaku 9KW SmartLab, Japan) was performed for crystal phase identification. Raman spectrum (confocal Raman microscope, Senterra R200-L, Bruker Optics) was also used to compare the crystallinity. The surface states were analyzed by X-ray photoelectron spectroscopy (XPS, AXIS Ultra, Japan) measurement using Al K α monochromatized radiation. Morphological and structural variations of the TNAs were observed by a field-emission scanning electron microscope (FESEM, FEI Sirion 200) and a transmission electron microscope (TEM, JEOL JEM-2100F). The J–V characteristics were measured by a sourcemeter (Model 2420, Keithley, USA) under AM 1.5G illumination (100 mW cm⁻²) provided by a 300 W solar simulator (Model 91160, Newport-Oriel Instruments, USA) with an AM 1.5 filter. The light intensity was calibrated using a silicon reference cell (NIST) equipped with KG5 window and a readout power meter. The IPCE was measured by an IPCE measurement kit (Newport-Oriel Instruments) with a 300 W Xe lamp (Model 66902), a monochromator (Model 74125),

and a power meter (Model 2931-C) equipped with a Si detector (Model 76175_71580). EIS was performed in the dark at various bias voltages with the CHI 660C electrochemical workstation (CH Instruments, USA). The magnitude of the alternative signal was 10 mV and the frequency ranged from 10⁻¹ to 10⁵ Hz.

Supporting Information

Supporting Information is available from the Wiley Online Library or from the author.

Acknowledgements

The work was supported by grants received from the Research Grants Council of the Hong Kong Special Administrative Region (Project Nos. PolyU5187/09E and PolyU5163/12E) and the Hong Kong Polytechnic University (Project Nos. A-SA76 and RT5W). It was also supported by the National Natural Science Foundation of China (Grant No. 61125503), the Foundation for Development of Science and Technology of Shanghai (Grant Nos. 11XD1402600 and 10JC1407200) and the municipal government of Guangzhou (Project Nos. 2010-kz-70 and 2011J5100001).

Received: March 27, 2013

Revised: May 9, 2013

Published online: June 21, 2013

- [1] P. Roy, D. Kim, K. Lee, E. Spiecker, P. Schmuki, *Nanoscale* **2010**, *2*, 45.
- [2] J. Lin, X. L. Liu, M. Guo, W. Lu, G. G. Zhang, L. M. Zhou, X. F. Chen, H. T. Huang, *Nanoscale* **2012**, *4*, 5148.
- [3] S. So, K. Lee, P. Schmuki, *J. Am. Chem. Soc.* **2012**, *134*, 11316.
- [4] K. Shankar, G. K. Mor, H. E. Prakasam, S. Yoriya, M. Paulose, O. K. Varghese, C. A. Grimes, *Nanotechnology* **2007**, *18*, 065707.
- [5] C.-T. Yip, M. Guo, H. T. Huang, L. M. Zhou, Y. Wang, C. J. Huang, *Nanoscale* **2012**, *4*, 448.
- [6] D. B. Kuang, J. Brillet, P. Chen, M. Takata, S. Uchida, H. Miura, K. Sumioka, S. M. Zakeeruddin, M. Grätzel, *ACS Nano* **2008**, *2*, 1113.
- [7] K. Shankar, J. Bandara, M. Paulose, H. Wietasch, O. K. Varghese, G. K. Mor, T. J. LaTempa, M. Thelakkat, C. A. Grimes, *Nano Lett.* **2008**, *8*, 1654.
- [8] O. K. Varghese, M. Paulose, C. A. Grimes, *Nat. Nanotechnol.* **2009**, *4*, 592.
- [9] D. Kim, A. Ghicov, S. P. Albu, P. Schmuki, *J. Am. Chem. Soc.* **2008**, *130*, 16454.
- [10] D. R. Baker, P. V. Kamat, *Adv. Funct. Mater.* **2009**, *19*, 805.
- [11] K. Zhu, N. R. Neale, A. Miedaner, A. J. Frank, *Nano Lett.* **2007**, *7*, 69.
- [12] C. Richter, C. A. Schmuttenmaer, *Nat. Nanotechnol.* **2010**, *5*, 769.
- [13] J. R. Jennings, A. Ghicov, L. M. Peter, P. Schmuki, A. B. Walker, *J. Am. Chem. Soc.* **2008**, *130*, 13364.
- [14] C.-J. Lin, W.-Y. Yu, S.-H. Chien, *J. Mater. Chem.* **2010**, *20*, 1073.
- [15] Y. Yu, K. J. Wu, D. L. Wang, *Appl. Phys. Lett.* **2011**, *99*, 192104.
- [16] A. Ghicov, S. P. Albu, R. Hahn, D. Kim, T. Stergiopoulos, J. Kunze, C. A. Schiller, P. Falaras, P. Schmuki, *Chem. Asian J.* **2009**, *4*, 520.
- [17] K. Zhu, N. R. Neale, A. F. Halverson, J. Y. Kim, A. J. Frank, *J. Phys. Chem. C* **2010**, *114*, 13433.
- [18] Y. Yang, X. H. Wang, L. T. Li, *J. Am. Ceram. Soc.* **2008**, *91*, 632.
- [19] K. L. Schulte, P. A. DeSario, K. A. Gray, *Appl. Catal. B* **2010**, *97*, 354.
- [20] L. J. Liu, J. Chan, T. K. Sham, *J. Phys. Chem. C* **2010**, *114*, 21353.

- [21] O. K. Varghese, D. W. Gong, M. Paulose, C. A. Grimes, E. C. Dickey, *J. Mater. Res.* **2003**, *18*, 156.
- [22] N. K. Allam, C. A. Grimes, *J. Phys. Chem. C* **2009**, *113*, 7996.
- [23] S. P. Albu, H. Tsuchiya, S. Fujimoto, P. Schmuki, *Eur. J. Inorg. Chem.* **2010**, *2010*, 4351.
- [24] Y. Sun, K. P. Yan, G. X. Wang, W. Guo, T. L. Ma, *J. Phys. Chem. C* **2011**, *115*, 12844.
- [25] J. G. Yu, B. Wang, *Appl. Catal. B* **2010**, *94*, 295.
- [26] Q. Ma, S. J. Liu, *Electrochim. Acta* **2011**, *56*, 7596.
- [27] J. Wang, L. Zhao, V. S. Y. Lin, Z. Q. Lin, *J. Mater. Chem.* **2009**, *19*, 3682.
- [28] D. Fang, Z. P. Luo, K. L. Huang, D. C. Lagoudas, *Appl. Surf. Sci.* **2011**, *257*, 6451.
- [29] J. Lin, J. F. Chen, X. F. Chen, *Electrochem. Commun.* **2010**, *12*, 1062.
- [30] J. Lin, K. Liu, X. F. Chen, *Small* **2011**, *7*, 1784.
- [31] C.-T. Yip, H. T. Huang, L. M. Zhou, K. Y. Xie, Y. Wang, T. H. Feng, J. Li, W. Y. Tam, *Adv. Mater.* **2011**, *23*, 5624.
- [32] M. Guo, K. Y. Xie, J. Lin, Z. H. Yong, C.-T. Yip, L. M. Zhou, Y. Wang, H. T. Huang, *Energy Environ. Sci.* **2012**, *5*, 9881.
- [33] W. F. Zhang, Y. L. He, M. S. Zhang, Z. Yin, Q. Chen, *J. Phys. D: Appl. Phys.* **2000**, *33*, 912.
- [34] V. Likodimos, T. Stergiopoulos, P. Falaras, J. Kunze, P. Schmuki, *J. Phys. Chem. C* **2008**, *112*, 12687.
- [35] J. Lin, X. F. Chen, *Phys. Status Solidi RRL* **2012**, *6*, 28.
- [36] Q. Wang, S. Ito, M. Grätzel, F. Fabregat-Santiago, I. Mora-Seró, J. Bisquert, T. Bessho, H. Imai, *J. Phys. Chem. B* **2006**, *110*, 25210.
- [37] F. Fabregat-Santiago, E. M. Bareja, J. Bisquert, G. K. Mor, K. Shankar, C. A. Grimes, *J. Am. Chem. Soc.* **2008**, *130*, 11312.
- [38] B. C. O'Regan, K. Bakker, J. Kroese, H. Smit, P. Sommeling, J. R. Durrant, *J. Phys. Chem. B* **2006**, *110*, 17155.
- [39] J. van de Lagemaat, A. J. Frank, *J. Phys. Chem. B* **2000**, *104*, 4292.
- [40] A. F. Halverson, K. Zhu, P. T. Erslev, J. Y. Kim, N. R. Neale, A. J. Frank, *Nano Lett.* **2012**, *12*, 2112.